Discovering Crystal Forms of the Novel Molecular Semiconductor OEG-BTBT

Priya Pandey, Nicola Demitri, Lara Gigli, Ann Maria James, Félix Devaux, Yves Henri Geerts, Enrico Modena,* and Lucia Maini*

ACCESS | Metrics & More | Article Recommendations | Supporting Information

ABSTRACT: This work is focused on a polymorphic and crystallographic study of a novel p-type organic semiconductor 2,7-bis(2-(2-methoxyethoxy)ethoxy)benzo[b]-benzo[4,5]thieno[2,3-d]thiophene (OEG-BTBT). The well-known BTBT core is functionalized by eight-atom-long oligoethylene glycol side chains. Our results demonstrate the discovery of three crystal forms of the OEG-BTBT molecule, namely, Form I, Form II, and Form III, in different experimental conditions. Crystal structures of Form I and Form III are reported, while only unit cell indexing of Form II could be determined. Form I and Form II are enantiotropically related, and Form II is stable at temperatures higher than 127 °C. The kinetics of transformation to Form II was studied by the Avrami equation. Form III is a solvate crystal form which is rarely observed in the field of organic electronics, and upon release of dichloromethane, it converts to Form I. Furthermore, we studied the mechanical properties of the Form I crystals, which exhibit plastic bending upon applying mechanical stress in the [100] direction. This distinct mechanical behavior is rationalized by the slip layer topology, the intermolecular interactions energies from energy frameworks, and the Hirshfeld surface analysis.
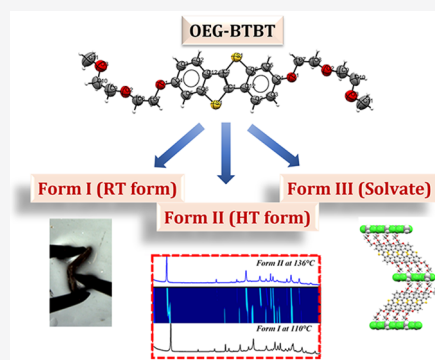
INTRODUCTION

Organic semiconductors (OSCs) have been widely studied in the past three decades fueled by their high versatility and large number of advantages in electronics owing to the merits such as solution-processability and the low cost of production.[1−4] While dealing with organic molecules, where weak van der Waals interactions prevails, it is expected that the molecules adapt different crystal packings, thus leading to polymorphism. This may induce variation in electronic, mechanical, or optical properties.[5−7]

A key property in OSCs is charge carrier mobility, which is defined as the derivative of the drift velocity of the charge carrier with respect to the applied electric field.[8] The changes in the charge carrier mobilities of OSCs depend on the crystal packing as the thermal fluctuations can disrupt the molecular order which causes an effect on the charge mobility.[2,9,10] It has been reported that even minor changes in the packing have a remarkable impact on the mobility, thereby affecting the electronic performances by orders of magnitude.[11,12] While polymorph screening is a well-established standard technique for pharmaceutical molecules, for organic electronics this technique is not widely popular in spite of a known fact that OSCs exist in different crystal forms[13,14] as observed in OSCs such as pentacene,[15−18] rubrene,[19] oligothiophene,[20,21] and [1]benzothieno[3,2-b]benzothiophene (BTBT) derivatives.[22,23] Polymorphism can serve as a great tool to enhance charge carrier mobilities without having to modify the

compound chemically.[24,25] So, it is very crucial to explore the different polymorphs of an organic molecular semiconductor to have a complete understanding of various packing arrangements that a molecule can adopt depending on its thermodynamic and kinetic behavior.[26] Understanding the packing also provides in-depth knowledge of the structure−property relationships.[27,28] The stability of the crystal forms should be investigated as well to avoid conversion upon storage. Polymorph prediction can support polymorph screening and gives important hints on the presence of stable forms; however, its complexity increases with the number of degrees of freedom of the studied molecule. The most stable form at room temperature, among the polymorphs known, can be easily determined by thermal and slurry experiments, although it does not guarantee that a more stable form could not be found later.[29−31]

BTBT derivatives are reported to have fairly good mobility values.[25,32] Substitutions and functionalization at 2 and 7 positions on BTBT core with various chains have been explored to understand the correlation of linear alkyl and bulky chains with the properties.[1,22,23,32,33,33−36] We wanted to inspect the

structural aspects and molecular packing arrangements of the molecule with an oligoethylene glycol functionalized chain, which should have a different set of chain—chain and chain-core interactions compared to that of alkyl chains of similar length.

In an attempt to reveal the structural attributes by ethylene glycol chain substitutions at the 2 and 7 positions of the BTBT core, we have investigated 2,7-bis(2-(2-methoxyethoxy)-ethoxy)benzo[b]benzo[4,5]thieno[2,3-d]thiophene (OEG-BTBT) (Figure 1) in this work, which is a p-type semiconductor
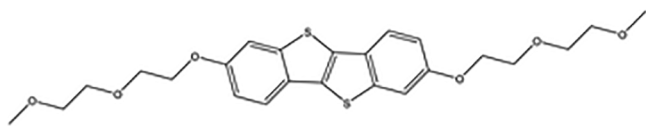

Figure 1. Chemical structure of OEG-BTBT.

molecule. On the account of the well-studied and well-performing C8-BTBT-C8,[37,38] we selected a similar and symmetric chain length of OEG in our study. One of the most critical tasks in the study of novel materials is the ability to anticipate and control the distinct properties in the solid state.[39] The packing of BTBT is driven by the core (which is responsible for the charge mobility) and by the chains.Length and steric hindrance of the alkyl chain play a key role in the final structure.[22,23,36] In OEG-BTBT, we would like to explore how the different polarities of the chain impact the molecular packing.

While dealing with organic molecular semiconductors and electronic properties, one must not disregard the importance of mechanical properties of the crystals of OSC. Generally, organic molecular crystals are fragile and exhibit brittle mechanical behavior. They tend to crack on mechanical impacts and therefore significantly limit the durability of the devices.[40,41] A crystal's response to applied mechanical stress is intrinsically linked to the molecular packing and the intermolecular interaction strengths.[42,43] This manuscript principally illustrates the structural and mechanical properties of the OEG-BTBT semiconductor molecule.

In this work, a series of experiments on polymorph screening starting from solubility tests were performed since it is evident that, at the molecular level, the solvent may have a profound impact on the nucleus structure through some solvent—molecule interactions that may govern the formation of a particular structure. Interestingly, after an intensive range of conditions were tested for this system, we discovered three crystal forms which are described in detail in later sections. The thermodynamically stable form at room temperature is Form I, while the high temperature form is called Form II. During the investigations of the solvent-induced polymorphs, we discovered a metastable solvate form in dichloromethane solvent, which is reported as Form III.[2,12] This finding is indeed interesting as the occurrence of solvate crystal forms in the OSCs is quite rare,[13] while it is common for active pharmaceutical ingredients (APIs).[44] Further future research is needed to understand if the rarity of solvates in OSCs is due to the intrinsic instability or the lack of research. The research herein focuses on a detailed analysis of these three crystal systems of the OEG-BTBT molecule.

■ EXPERIMENTAL SECTION

Polymorph Screening. Solubility screening was performed for OEG-BTBT using 25 different solvents prior to further study (Table

S1). Solubility was examined at room temperature (RT) and 50 and 75 °C (depending on the boiling point of solvents). Recrystallization was carried out by solvent evaporation at RT in chloroform (CHF), dichloromethane (DCM), N,N-dimethylacetamide (DMA), N,N-dimethylformamide (DMF), cyclohexanone, toluene (TOL), and tetrahydrofuran (THF). Antiprecipitation from supersaturated solutions was carried out with chloroform/propyl acetate (1:1) and dichloromethane/1,4-dioxane (1:1). Crystallization through the solvothermal technique was performed using CHF and DCM. All precipitates were characterized by PXRD. In all of the experiments, Form I was obtained except in DCM where we obtained Form III.

Single-Crystal X-ray Diffraction (SCXRD). Suitable crystals of Form I and Form III for single-crystal X-ray diffraction were obtained from CHF and DCM solutions (1 mg/mL), respectively.

Data collection of room temperature (298 K) Form I OEG-BTBT was performed at the X-ray diffraction beamline (XRD2) of the Elettra Synchrotron, Trieste, Italy.[45] Small, rodlike crystals were grown on the silicon wafer. Single crystals were dipped in NHV oil (Jena Bioscience, Jena, Germany) and mounted on a goniometer head with Kapton loops (MiTeGen, Ithaca, USA), using a 50 μm aperture. Data were acquired using a monochromatic wavelength of 0.620 Å on a Pilus 6M hybrid-Pixel area detector (DECTRIS Ltd., Baden-Daettwil, Switzerland) at a working distance of 185 mm, using MXCuBE3 control software.[46] Form I and Form III at low temperature (100 K) SCXRD was performed by a Bruker Apex-II diffractometer with a Photon II detector. Low-temperature data were collected for Form I and Form III with the Bruker APEX2 program, and integrated and reduced with the Bruker SAINT software.

Low-temperature data (100 K) are still consistent with the room temperature model of Form I (i.e., no detectable phase transition has been detected upon flash cooling in liquid nitrogen).

Form I (LT and RT) and Form III crystal structures were solved using WingX software SHELXS and SHELXT codes and refined with SHELXL (version 2018/3).

For visualization, pictures of crystal structures from CCDC Mercury 2020.3.0 were used.[47,48]

Powder X-ray Diffraction (PXRD). Qualitative PXRD to identify the crystalline form were collected with a Rigaku MiniFlex 600 diffractometer with Cu Kα radiation from a copper-sealed tube with 40 kV voltage and 15 mA current in Bragg—Brentano geometry. Diffraction patterns were measured over the range of 3–40° 2θ by step scanning at a rate of 1 s/0.01°.

Thermogravimetric Analysis-Evolved Gas Analysis (TGA-EGA). TGA-EGA was performed on Mettler-Toledo TGA coupled with a Thermo Nicolet iS 10IR FT_IR spectrometer with a scan rate of 10 °C/min and analyzed using STARe software.

Differential Scanning Calorimetry (DSC). The DSC for all of the samples was performed on a Mettler-Toledo DSC1 instrument. About 2–4 mg of samples was crimped in hermetic aluminum crucibles (40 μL) and scanned from room temperature to 300 °C at a heating rate 10 °C/min under a dry N$_2$ atmosphere (flow rate 80 mL/min) for Form I and Form III. The data were dealt with using STARe software.

In-Situ Variable Temperature X-ray Diffraction (VTXRD). VTXRD was performed at the Paul Scherrer Institut (PSI) Synchrotron radiation facility (Switzerland) using PXRD in the capillary transmission mode at MS-X04SA beamline from 20 to 136 °C. The beam energy of 12.4 keV (1.0 Å) was used for data collection. The MS powder diffractometer in Debye—Scherrer geometry, equipped with a solid-state silicon microstrip detector, called MYTHEN (Microstrip sYstem for Time-rEsolved experimeNts) was utilized. Starting from room temperature, the XRD pattern was collected at various intervals until complete conversion of Form I to Form II (136 °C).[49]

Hot Stage Microscopy (HSM). Single crystals on a glass-slide and covered with a coverslip were placed in a heating chamber (hot stage) on an OLYMPUS BX41 stereo-microscope equipped with an LINKAM LTS350 platinum plate for temperature control and VISICAM analyzer. The heating chamber was capped with a sealable lid during heating and cooling cycles, and the rate was kept constant at 10 °C min^{-1}. Time-lapse images were taken using a Nikon DS FI3 high speed

camera for all in-situ experiments, and the images were analyzed using software Nikon NIS Elements and Linksys32 data capture.

Attenuated Total Reflection-Fourier Transform Infrared (ATR-FTIR) and Raman Spectroscopy. Infrared spectra of the crystals of OEG-BTBT were obtained using a Fourier−transformation infrared spectrometer (spectrometer: Nicolet iS50 and detector: DTGS ATR). The spectra were measured over the range of 4000−400 cm^{-1}. For Raman spectroscopy, a Raman confocal imaging microscope with a HeNe laser (laser with a maximum power 100−240 V 50/60 Hz) was used.

We employed the ATR-FTIR measurement on both Form I and Form III of OEG-BTBT crystals. On comparing both the forms, Form III was found to have signals of both Form I and DCM, which further confirms our previous analysis for solvate Form III (Figure S6).

Mechanical Deformation Tests. Mechanical bending tests on the single crystals of OEG-BTBT were performed on a stereo-microscope equipped with cross polarizers and a Nikon DS-Fi3 camera using a needle and forceps.

Hirshfeld Surface Analysis. The package CrystalExplorer 17.5 was used for the Hirshfeld surface analysis on each of the forms. The analysis was carried out based on their respective crystal geometries. The corresponding 2D fingerprint plots were also generated using CrystalExplorer 17.5.

Energy Frameworks Analysis and Interaction Energy Calculations. CrystalExplorer 17.5 was used to evaluate and visualize the pairwise interaction energies of OEG-BTBT Forms. The tube size (scale factor) used in all the energy frameworks was 100, and the lower energy threshold (cut off) value was set to 5 kJ/mol. The energy components calculated within this method are electrostatic, polarization, dispersion, and exchange-repulsion and finally the total interaction energy. These energy calculations are accomplished at the B3LYP/6-31G(d,p) level of theory and using crystal geometries (experimental structures) of the respective forms.

RESULTS AND DISCUSSION

Polymorph Screening. Solubility tests show that OEG-BTBT is highly insoluble in most of the organic solvents, except in CHF, DCM, DMA, DMF, TOL, THF, and cyclohexanone.

OEG-BTBT is a crystalline material, and it was recrystallized in the various solvents mentioned above and, in all cases, yielded to the formation of the starting crystalline material called Form I, while by recrystallization of OEG-BTBT in DCM, the solvate crystal form called Form III, was obtained concomitantly with Form I (Figure S4). Surprisingly, after many attempts, no Form III was obtained by prolonged slurry experiments in DCM. However, we were able to obtain the single-crystal structure of Form III at 100 K (see below).

In addition to recrystallization from solution, other methods to explore the polymorphs were investigated, such as the solvothermal method in CHF and DCM, precipitation at gradient temperature, antisolvent crystallization, slurry, and mechanochemistry. All of these experiments and different experimental conditions resulted in Form I, and no amorphous phase was detected.

Thermal Analysis. TGA and EGA analysis revealed that Form I is anhydrous and Form III is a solvate Form (Figure S1), and the DCM molecules are easily lost from the crystal lattice at high temperatures (48 °C) or at room temperature in less than seven days' time (Figures S2, S3 and S5).

The DSC curve of Form I revealed that there is a solid−solid reversible transition at around 127 °C (ΔH = 27.96 kJ/mol) confirmed also by the VTXRD at synchrotron, whereas the melting starts at 153 °C (ΔH = 22.76 kJ/mol) (Figure 2a). Upon cooling from the melt, first, we observe Form II at a higher temperature, which converts to Form I, and this shows the reversible behavior of the solid−solid transition. It is worth
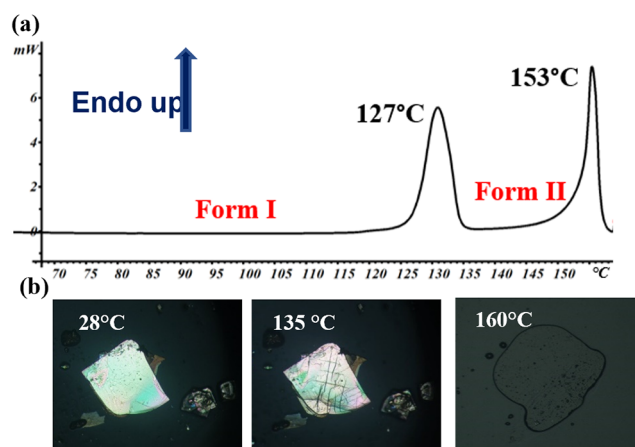

Figure 2. OEG-BTBT Form I (a) DSC plot showing the onset temperature of the transition and melting (Endo UP), (b) HSM showing transition at 135 °C and melt at 160 °C. The heating rate for both DSC and HSM was 10 °C/min.

noting that the energy involved in the solid−solid transition is higher than the energy involved in the melting, which suggests that Form II is a disordered phase, and most heat stored in the crystal is exchanged during solid−solid transitions rather than at melting. In the DSC curve of Form III crystals (Figure S3), a small endothermic peak near 48 °C is clearly visible, which indicates the loss of DCM solvent, whereafter Form III solvate converts to the pristine Form I as the thermal behavior after the first peak is identical to Form I DSC.

The thermal transitions were also monitored by hot stage microscopy (HSM) experiments to observe the morphological changes taking place as a result of the thermal energy input. Form I crystal starts to convert at 129 °C, and the crystal shows cracks and changes on light polarization, but the crystallinity is highly maintained (Figure 2b).

The HSM of Form III visually confirms the onset of release of solvent at around 75 °C. Interestingly, it is not a destructive transition as commonly observed, and it converts into Form I, and then the conversion into Form II is observed to start at 125 °C and the melting at 140 °C. By cooling the melt, Form II crystallizes, which exhibits a reversible transition at 125 °C resulting in the stable polymorph (Form I) at room temperature (Video S1).

Crystal Structure Analysis of Polymorphs. Crystallization of the OEG-BTBT compound leads to mainly flat and thin crystals with plate-like morphology when subjected to very slow evaporation. Form I crystal data were collected at room temperature (RT) and low temperature (LT); it is monoclinic with space group $P2_1/c$ and a half molecule in the asymmetric unit, and the inversion center generates the whole molecule (see Table 1).

The molecule is characterized by the flat rigid core and the flexible oligoether chain, which is almost perpendicular to the core. The chain, due to the presence of the oxygen, loses the regularity of the alkyne chain with the formation of a torsion angles (O−C−C−O) in the range 68.66(8)−70.29(7)°, which is close to the average value of the torsion angle of ethylene glycol statistics obtained from Mogul software (Figure S9).[50] As observed in most BTBT systems, the OEG-BTBT molecules form a herringbone packing motif with an angle of 52.74° (LT) and 53.01° (RT) and short contact face-to-edge interactions S−C. In fact, the sulfur atom interacts with two carbon atoms

Table 1. Cell Parameters of Form I (RT and LT), Form II, and Form III (LT)

| parameters	Form I (298 K)	Form I (100 K)	Form II (404 K)	Form III (100 K)
formula		$C_{24}H_{28}O_6S_2$		$C_{24}H_{28}O_6S_2$, CH_2Cl_2
molecular weight (g mol^{-1})		476.58		561.51
crystal system	monoclinic	monoclinic	monoclinic	orthorhombic
space group	$P2_1/c$ (14)	$P2_1/c$ (14)	C	$Pnma$ (62)
a (Å)	18.635(4)	18.407(2)	11.653	8.303(1)
b (Å)	7.667(2)	7.607(1)	41.255	41.759(1)
c (Å)	8.293(2)	8.202(1)	8.338	7.491(1)
β (deg)	99.35(3)	100.423(4)	64.552	90.000
V (Å^3)	1169.1 (4)	1129.6(2)	3619.745	2597.3(1)
Z/Z′	4/0.5	4/0.5	6/1.5	8/0.5
density (g·cm^{-3})	1.354	1.401	1.311	1.436
$F(000)$	504.0	504.0		1176.0
μ (mm^{-1})	0.183	2.468		4.083
GOF on F^2	0.996	1.216		1.021
R_1 (on F, $I > 2\sigma(I)/R_{ex}$)	0.103	0−097		0.031
wR_2 (F^2 all data) R_{wp}	0.237	0.264		0.075
CCDC no.	2109678	2109679		2109680
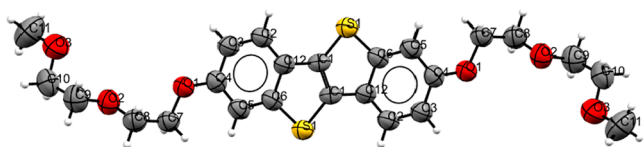
Figure 3. Crystal structure of Form I (RT).

having a distance of 3.374(2) Å and 3.440(2) Å (LT). The twisted chains are involved in short O−H contacts as also highlighted by the Hirshfield calculation (see below).

The intermolecular interactions which take place organizes the molecules in parallel to form layers, which are characterized by the inner part occupied by the aromatic core and the surface by the OEG chains. If the core of the molecule is described by the vector as shown in Figure 4c, it is easy to observe that all the parallel molecules have a tilt angle of 60.32° with respect to the
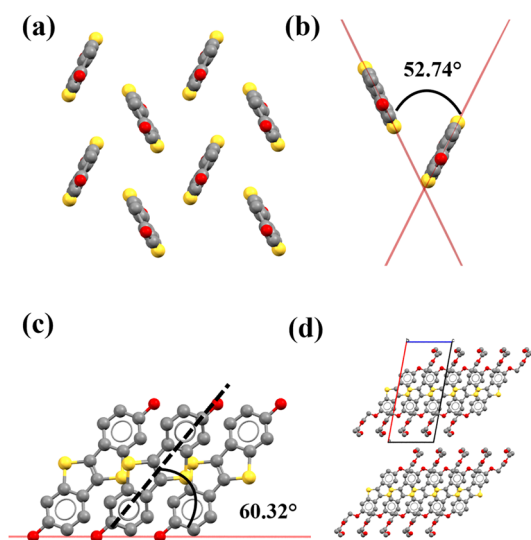

Figure 4. Form I (a) herringbone packing arrangement of the core, (b) herringbone angle of the core, (c) core-tilt angle, and (d) packing (2 × 2 × 2) along the *b*-axis, showing the parallel arrangement of layers. For simplicity, the OEG chains from (a−c) and hydrogens in (d) are deleted.

(1 0 0) face. These layers are stacked one over the other, and in the case of Form I the molecules are parallelly arranged also in interlayers (Figure 4d).

Form III crystallizes as orthorhombic with space group *Pnma* and half a OEG-BTBT molecule and half a solvent molecule in the asymmetric unit. The whole OEG-BTBT molecule is generated by the inversion center, while the solvent molecule lies on the mirror plane. Despite the possibility of having different chain configurations, the OEG-BTBT molecules in Form I and Form III are superimposable with root-mean-square deviation (RMSD, defined as the square root of the mean squared error, commonly used for analyzing packing similarities[48,51]) of 0.023 Å for one molecule (Figure 5), while for 15 molecules, it is 0.141 Å (Figure S15).
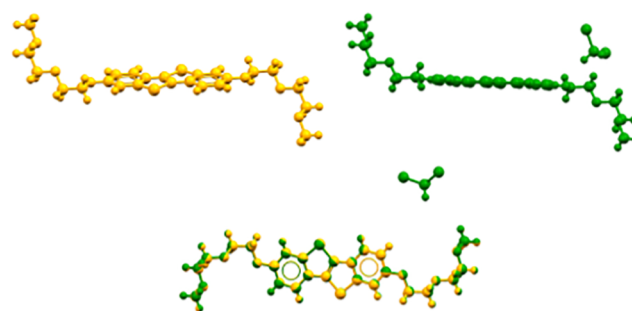

Figure 5. Superimposition of Form I and Form III with a RMSD of 0.023 Å.

Similar to Form I, Form III also has a herringbone packing motif of the core with the herringbone angle 50.62° and which forms layers stacking along the *b*-axis. Form III also exhibits face-edge short contacts between S−C having a distance of 3.371(2) Å and 3.406(2) Å, which are slightly shorter than in Form I due to the smaller angle.

Form III molecules are also arranged in layers as in Form I, but in this case the layers are antiparallel to each other with the solvent molecule in between them (Figure 6d). The solvent molecules which are placed between the layers of OEG-BTBT are involved only in weak interactions with the oligoether chains and among themselves. Because of the solvent contribution,
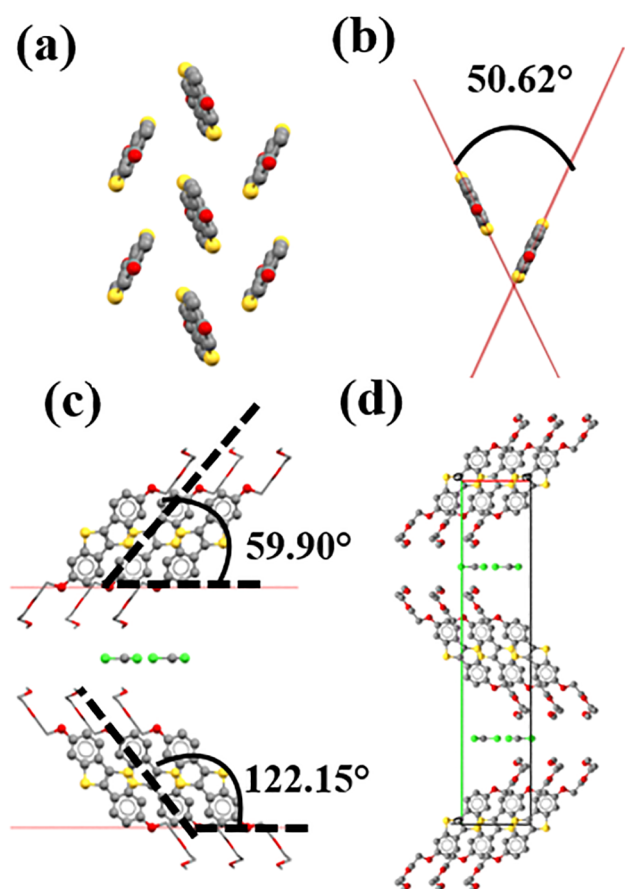
Figure 6. Form III (a) herringbone packing arrangement of the core, (b) herringbone angle of the core, (c) core-tilt angle, and (d) packing along the *b*-axis, showing the antiparallel arrangement of layers. For simplicity, the OEG chains in (a−b) and hydrogens in (c−d) are deleted.

there are a greater number of short contacts in Form III when compared to Form I (RT and LT). A comparative list of all the short contacts is depicted in Table S2 and Figure S12. As the solvent molecule disappears from the structure, the molecular packing loosens, due to which the molecules reorient themselves back to the original Form I.

Form II is stable at a temperature higher than 134 °C before melting, so no single-crystal data could be collected. However, we were able to determine the unit cell of Form II using the powder XRD pattern collected at the PSI synchrotron. The pattern was indexed using TOPAS (Figure S14) and was found to have a monoclinic crystal structure (C2) having the unit cell parameters $a = 11.653$ Å, $b = 41.255$ Å, $c = 8.338$ Å, $\beta = 64.552°$, and volume 3619.745 Å^{-3}, which corresponds to the presence of one and a half molecules in an asymmetric unit. The strong peak at a low angle (2.77°) suggests the presence of layers as observed in Form I and Form III. The distance between the layers increases from 18.37 Å in Form I (at 110 °C) to 20.59 Å in Form II, which could be due to the core-tilt angle or the straightening of the chain. Despite numerous attempts, it was not possible to solve the structure of Form II, maybe due to the high number of degrees of freedom (30 DoF) and/or by the presence of disorder. Taking evidence from the DSC plot, the higher enthalpy of transition with respect to the enthalpy of fusion indicates the presence of a disordered phase of Form II.

Hirshfeld Surface Analysis. For 3D visualization and clear understanding of intermolecular interactions, Hirshfeld surfaces and their respective 2D fingerprint plots were calculated using Crystal Explorer.[52] The electron density Hirshfeld surface plot of Form I was mapped over d_{norm} with the range of −0.1025 to 1.4721, and −0.1732 to 1.2442 for Form III. The d_{norm} plots were chosen for mapping since they combines both the distance from the point to the nearest nucleus external to the surface (d_e) and the distance to the nearest nucleus internal to the surface (d_i), each normalized by the van der Waals radius for the particular atoms involved in the close contact to the surface.[1,52]

The plot clearly indicates the dominant interactions with the red-colored spots, which denotes the distance shorter than the van der Waals distance. Form I at LT exhibits a total of 10 red regions of d_{norm}, 4 C−S and 6 O−H red regions (Figure 7a),
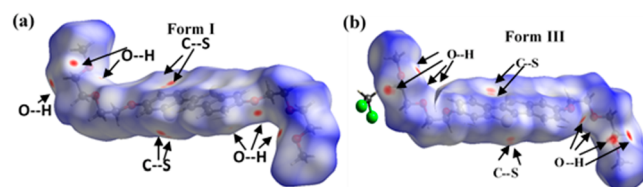

Figure 7. Hirshfeld plot of OEG-BTBT (a) Form I mapped over d_{norm} −0.1025 to 1.4721 and (b) Form III mapped over d_{norm} −0.1732 to 1.2442. (Arrows indicate the d_{norm} short contacts in OEG-BTBT molecules; solvent interaction in (b) is not visible in this viewing direction.)

while Form III also possesses 14 major red regions containing 4 C−S and 6 red regions associated with O−H interactions from OEG-BTBT molecule and 4 O−H interactions of the OEG-BTBT and solvent molecule (Figure 7b).

The 2D fingerprint plots have proven to be highly useful for the identification of all of the short contact interactions. The single pointed spike in the middle of the fingerprint plot and the two spikes are indicative of the H−H and O−H interactions respectively, while the two wings and the inner part are due to the C−C and C−S interactions, respectively. C−H and C−S interactions are ascribable to the core of the molecules with a herringbone motif, and their plots are almost identical in the two forms, as seen in Figure 8, which confirms the similarity of the packing. Although they contribute only 25% of overall interactions, they are the driving force in the packing arrangement. In fact, the energy frameworks calculation indicates that the stronger interaction is among the molecules involved in the herringbone motif (see later). This surface analysis also reveals the absence of π−π contacts. The main differences are observed only in the H−H interactions, and small variations in O−H, which correspond to the chain as highlighted by the superimposition of the fingerprint plots (Figure S13). The H−H interactions are clearly hampered by the increased number of the O−H interactions in Form III due to interactions with the solvent.

In-Situ Variable -Temperature X-ray Diffraction-Kinetics Transformation. The VTXRDs of Form I were collected at the PSI synchrotron. The diffractograms were collected at regular intervals up to 136 °C. The transition was observed in the range of 117−131 °C (Figure 9).

To determine the solid-state kinetics, we rapidly heated Form I up to 121 °C, which corresponds to the temperature of transition, and collected the pattern at isothermal conditions. The diffractogram collected shows the presence of a mixed
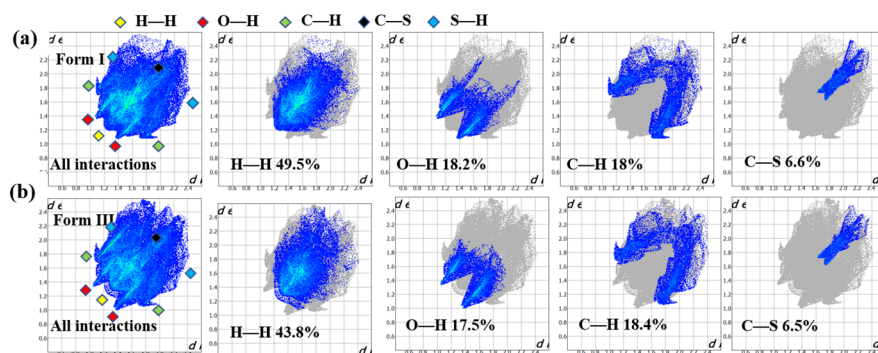
Figure 8. Hirshfeld surface fingerprint plots of (a) Form I and (b) Form III, showing percentage contributions of H−H, O−H, and C−H interactions. The regions in the first plot are marked with different colors for easy identification of the respective interactions.
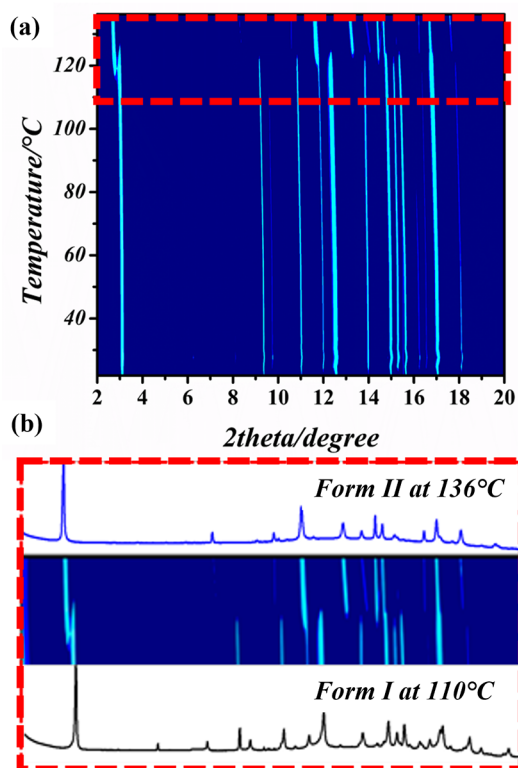

Figure 9. VTXRD of OEG-BTBT at the PSI synchrotron (a) 2D isolines view of the temperature range of 20−136 °C, (b) 2D isolines zoomed in the transition region and compared with the respective diffraction.

phase in the start and finally corresponds to Form II. The quantification of the emergence of Form II was determined using the PONKCS (partial or no known crystalline structures) method. The quantification depends on the derivation of the calibration factor of each phase that is present in the mixture.[53] The weight of each phase is proportional to the product of the scale factor. The weight fraction (W) of phase (p) is be written as

$$Wp = (Sp(ZMV)p) / \left(\sum i[Si(ZMV)i] \right) \tag{1}$$

where Z, M, V, and S are the number of formula units per unit cell, mass of the formula unit, unit volume, and the scale factor, respectively.[54] Hence, for each phase p, $(ZMV)_p$ is the "phase constant". We quantified the weight fractions of Form I and

Form II as a function of time, which indicates that with Form II increasing in weight fraction, Form I decreases simultaneously.

The rate coefficient depending on the crystal composition was evaluated by the general equation for determination of solid-state reaction kinetics, called the JMAK kinetic model (Johnson, Mehl, Avrami, and Kolmogorov).[55,56] This model can be used as a physical model of a crystalline phase fraction which is continually growing.[57] It is a fact that the S-shape of sigmoidal graph (Figure 10b) is attributable to the slow rate initially, which is due to the time required to form the nuclei of Form II and to start the growth. The transition is faster in the middle since the nuclei then grows into particles of Form II, while the nucleation continues in Form I. And finally, the rate becomes slow again in the end as there remains very few untransformed Form I, and thus the transformation reaches completion. A straight line least-squares fit of $\ln[\ln(1/(1 − W_p))]$ versus $\ln t$ (eq 3), where W_p is the extent of the reaction at time t at 121 °C, yielded a slope $n = 2.26$ and an y-intercept $\ln K = −4.73$. The slope (n) gives information about the kinetics, and it depends on the temperature.

$$Wp = 1 − \exp[−Kt]n \tag{2}$$

This equation can be written as

$$\ln[[\ln[(1/(1 − Wp))] = \ln K + n \ln t]] \tag{3}$$

The value of n must be an integer varying between 1 and 4. When $n = 4$, there is contribution from three-dimensions of growth, while when the distribution of nucleation sites becomes nonrandom, the value of n could become 1 or 2. Therefore, it is known that $n = 2$ is consistent with nucleation and one-dimensional growth processes.

Similar plots for slightly lower (117 °C) and higher (124 °C) temperatures were also studied (Figure S15). We observed that as the temperature increased from 117 to 124 °C, the value of the Avrami constant decreased from 3.81 to 1.33, indicating that the nucleation to growth ratio was decreasing. The Avrami constant is higher at lower temperature since the nucleation was occurring in all three directions randomly, and the growth was unhindered in the beginning, which led to a high value of n (3.81). But as the temperature was increased, the value of n went lower indicating two- and/or one-dimensional growth (Figure S15c,d).

Mechanical Deformation Tests. We tested the mechanical properties of Form I since Form II and III cannot be used in devices due to their metastability at RT. The crystals of Form I present a plate morphology, and the main faces are $(1\,0\,0)$ and $(\overline{1}\,0\,0)$. The analysis of the crystal packing revealed that there is a
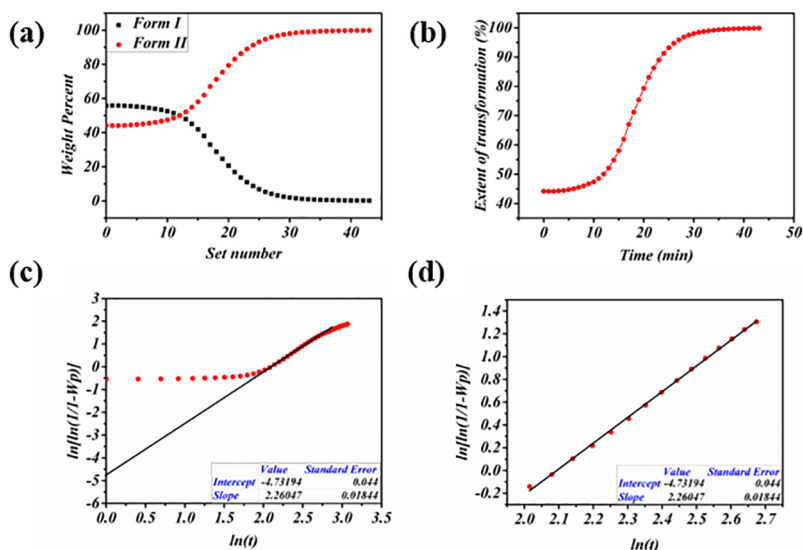
Figure 10. (a) The weight fractions of decaying Form I and emerging Form II, (b) sigmoid plot of the Avrami equation indicating the extent of transformation of Form II with time, (c) linear Avrami equation plot at 121 °C with slope = 2.26 and intercept = −4.73, and (d) zoom of the linear region of (c).
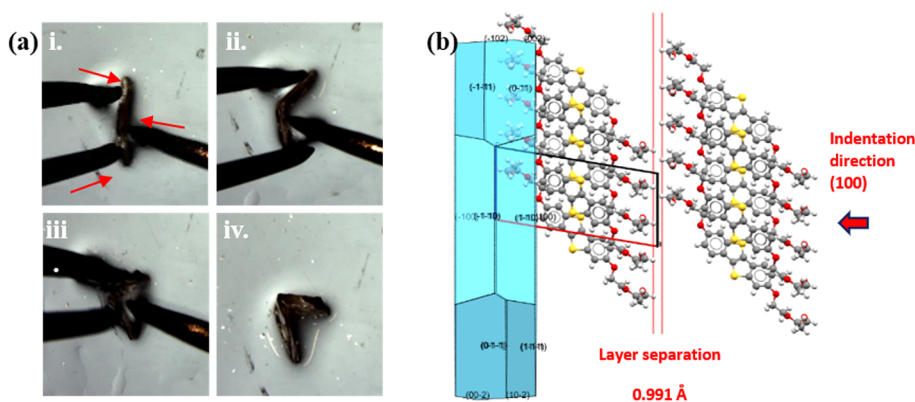

Figure 11. (a) (i−iv) Mechanical deformation tests of OEG-BTBT Form I crystals under an optical microscope, (b) BFDH morphology with packing showing the layer separation along the indentation direction (the crystal was held in the corner by forceps and pushed in the middle by a needle).

slip plane present in Form I with a molecular layer separation of 0.991 Å parallel to theses faces which may account for a bending characteristic of the crystals. On this account, we performed mechanical deformation tests on the suitable crystals perpendicular to the [1 0 0] direction using a needle and forceps. We clearly observed a plastic bending behavior of the OEG-BTBT Form I crystals, and it undergoes to an almost complete plastic behavior until the needle's diameter (Figure 11a,i–iv), whereas in deformation tests along other directions, it led to the breakage of crystals. This type of observed bending deformation is intrinsic to this material and not artifacts of extrinsic factors like particle shape and morphology.[42] The observed bending confirmed that molecular packing is fundamental for plastic behavior, which is facilitated by the energetically favored slip plane.

Usually, the organic crystals exhibit brittle behavior which leads to poor contacts with other components of the device since they might develop cracks upon mechanical impact which highly impacts the device durability.[58] Therefore, our system with anisotropic plasticity can prove to be advantageous for device applications.

Energy Framework Analysis. In order to rationalize the plastic deformation of the Form I crystals, the intermolecular energies and topology were analyzed using "energy frameworks" which offers an intelligent way to visualize the supramolecular architecture of molecular crystal structures.[59−61] We calculated the pairwise interaction energies of the Form I crystal structure which allowed us to investigate the 3D topology of the packing. The highest intermolecular interaction is −73.8 kJ/mol along the herringbone direction, while it is −39 kJ/mol in the stacking direction. Along the slip direction of the tapes [1 0 0], the intermolecular interaction energies were found to be the lowest (−3.7 kJ/mol and −4.9 kJ/mol), while in the intratape interactions are the highest, thus forming a 2D network (Figures S16 and S17). Therefore, this suggests that the weakest plane, (1 0 0) in this case, can act like a slip plane which allows the molecular layers to slide along.[62,63] With the mechanical impact in the direction of the 2D network (b-axis, (1 0 0) plane), the interaction energy of the molecules is strong enough to avoid the breakage; rather, it allows the bending by the aid of the slippage of the plane which is present between the two layers, thus keeping the layer interactions intact. It is evident that in molecular solids, bending occurs when there is a significant

difference in the strength of the intermolecular interactions in orthogonal directions.[64] From the energy frameworks, the same phenomenon is observed in the case of OEG-BTBT Form I (Figure 12).
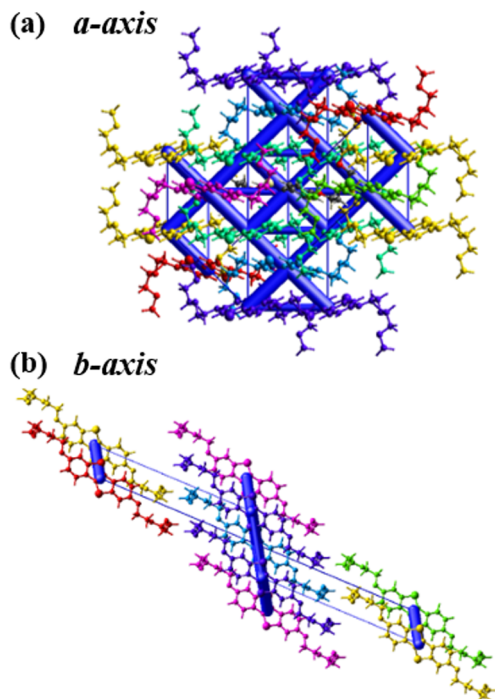

Figure 12. Energy frameworks corresponding to the total energy component in Form I along the (a) *a* and (b) *b* crystallographic axes. The energy scale factor is 25, and the energy threshold is 5 kJ mol^{-1}.

CONCLUSION

To summarize, we have reported the first detailed polymorphic study of BTBT core functionalized with oligoethylene glycol chains at 2 and 7 positions (OEG-BTBT). The polymorphic and structural investigation carried out for this system reveals the presence of three crystal forms. The thermodynamically stable Form I structure dominates since Form II and Form III are metastable at RT. Form II, which is a high-temperature polymorph, exists only at a temperature above 127 °C and below the melting point (153 °C). It was not possible to determine the crystal structure of Form II, but the energy involved in the phase transitions suggests that Form II is a disordered phase. We tried to understand the kinetics of transformation from Form I to Form II using the Avrami equation. At 121 °C, when the transformation was completed with increasing time, the value of the Avrami constant from the slope of the straight line was determined to be nearly 2, which denotes one-dimensional growth. Form III, which is a solvate of dichloromethane, found at ambient conditions again converts back to Form I as the DCM dries out of the crystal lattice (upon heating or within seven days of time). Both Form I and Form III were found to have herringbone packing motifs, although the packing differs in the arrangement of the adjacent tapes. Form I layers run parallel to each other, while Form III layers are arranged in an antiparallel fashion, with DCM molecules between them. The structural differences can also be seen in the short contacts and in Hirshfeld plots. However, in spite of the structural differences, the two molecules are superimposable.

Furthermore, mechanical properties were tested for Form I crystals, which revealed that Form I exhibits anisotropic plastic bending. This mechanical behavior turns out to be an additional benefit of our system in terms of organic electronics. Since most organic molecules exhibit brittle or elastic behavior, plastic crystals in our case offer a great advantage for better and flexible devices in the future. The presence of different polymorphic forms is common in the BTBT systems, and several studies suggest the active role of the chain on the crystal structure and also on the final applications.[22,32,36,65] Up to now, it is still challenging to design a material with the desired properties because it is difficult to control the final packing. Increasing the number of known structures increases the possibilities to rationalize the role of the chains for the packing.

■ ASSOCIATED CONTENT

ⓈI Supporting Information

The Supporting Information is available free of charge at https://pubs.acs.org/doi/10.1021/acs.cgd.1c01203.

> Figures related to PXRD, TGA-EGA, DSC, IR, UV patterns and indexing of the synchrotron powder diffractogram of compound OEG-BTBT along with different structural figures, tables, and energy calculations related to the crystal structures (PDF)

> Video S1 showing the phase transitions in Form III by hot stage microscopy (MP4)

Accession Codes

CCDC 2109678−2109680 contain the supplementary crystallographic data for this paper. These data can be obtained free of charge via www.ccdc.cam.ac.uk/data_request/cif, or by emailing data_request@ccdc.cam.ac.uk, or by contacting The Cambridge Crystallographic Data Centre, 12 Union Road, Cambridge CB2 1EZ, UK; fax: +44 1223 336033.

■ AUTHOR INFORMATION

Corresponding Authors

Enrico Modena — *PolyCrystalLine SPA, 29 40059 Bologna, Italy*; Email: enrico.modena@polycrystalline.it

Lucia Maini — *Dipartimento di Chimica "G. Ciamician", via Selmi 2 — Università di Bologna, I-40126 Bologna, Italy*; ⓞ orcid.org/0000-0002-0703-2617; Email: l.maini@unibo.it

Authors

Priya Pandey — *PolyCrystalLine SPA, 29 40059 Bologna, Italy; Dipartimento di Chimica "G. Ciamician", via Selmi 2 — Università di Bologna, I-40126 Bologna, Italy*

Nicola Demitri — *Elettra Sincrotrone Trieste, I-34149 Trieste, Italy*; ⓞ orcid.org/0000-0003-0288-3233

Lara Gigli — *Elettra Sincrotrone Trieste, I-34149 Trieste, Italy*

Ann Maria James — *Institute of Solid-State Physics, Graz University of Technology, 8010 Graz, Austria*

Félix Devaux — *Laboratoire de Chimie des Polymères, Faculté des Sciences, Université Libre de Bruxelles (ULB), 1050 Bruxelles, Belgium*

Yves Henri Geerts — *Laboratoire de Chimie des Polymères, Faculté des Sciences, Université Libre de Bruxelles (ULB), 1050 Bruxelles, Belgium; International Solvay Institutes, Université Libre de Bruxelles (ULB), 1050 Bruxelles, Belgium*; ⓞ orcid.org/0000-0002-2660-5767

Complete contact information is available at:
https://pubs.acs.org/10.1021/acs.cgd.1c01203

Author Contributions

P.P.: Investigation, experimental and computational analysis, and writing the manuscript. N.D. and L.G.: Collection and solution of single-crystal data of Form I (room temperature) crystal structure. A.M.J.: Handling of Form I RT crystal structure and discussion. F.D.: Synthesis and supply of the OEG-BTBT starting material. Y.H.G.: Supervision, manuscript review, and editing. E.M.: Conceptualization and supervision. L.M.: Supervision, manuscript review, and editing.

Notes

The authors declare no competing financial interest.

■ ABBREVIATIONS

OSCs, organic semiconductors; OEG-BTBT, 2,7-bis(2-(2-methoxyethoxy)ethoxy)benzo[b]benzo[4,5]thieno[2,3-d]-thiophene (OEG-BTBT); CHF, chloroform; DCM, dichloromethane; DMA, N,N-dimethylacetamide; DMF, N,N-dimethylformamide; TOL, toluene and THF, tetrahydrofuran; RT, room temperature; LT, low temperature; SCXRD, single-crystal X-ray diffraction; PXRD, powder X-ray diffraction; TGA-EGA, thermogravimetric analysis-evolved gas analysis; DSC, differential scanning calorimetry; VTXRD, in-situ variable temperature X-ray diffraction; HSM, hot stage microscopy; ATR-FTIR, attenuated total reflection-Fourier transform infrared

■ REFERENCES

(1) Roche, G. H.; Tsai, Y.-T.; Clevers, S.; Thuau, D.; Castet, F.; Geerts, Y. H.; Moreau, J. J. E.; Wantz, G.; Dautel, O. J. The Role of H-Bonds in the Solid State Organization of [1]Benzothieno[3,2-b][1]Benzothiophene (BTBT) Structures: Bis(Hydroxy-Hexyl)-BTBT, as a Functional Derivative Offering Efficient Air Stable Organic Field Effect Transistors (OFETs). *J. Mater. Chem. C* **2016**, *4* (28), 6742−6749.

(2) Chung, H.; Diao, Y. Polymorphism as an Emerging Design Strategy for High Performance Organic Electronics. *J. Mater. Chem. C* **2016**, *4* (18), 3915−3933.

(3) Ruzié, C.; Karpinska, J.; Laurent, A.; Sanguinet, L.; Hunter, S.; Anthopoulos, T. D.; Lemaur, V.; Cornil, J.; Kennedy, A. R.; Fenwick, O.; Samorì, P.; Schweicher, G.; Chattopadhyay, B.; Geerts, Y. H. Design, Synthesis, Chemical Stability, Packing, Cyclic Voltammetry, Ionisation Potential, and Charge Transport of [1]Benzothieno[3,2-b][1]Benzothiophene Derivatives. *J. Mater. Chem. C* **2016**, *4* (22), 4863−4879.

(4) Maini, L.; Gallino, F.; Zambianchi, M.; Durso, M.; Gazzano, M.; Rubini, K.; Gentili, D.; Manet, I.; Muccini, M.; Toffanin, S.; Cavallini, M.; Melucci, M. Chemical Design Enables the Control of Conformational Polymorphism in Functional 2,3-Thieno(Bis)Imide-Ended Materials. *Chem. Commun.* **2015**, *51* (11), 2033−2035.

(5) Devarapalli, R.; Kadambi, S. B.; Chen, C.-T.; Krishna, G. R.; Kammari, B. R.; Buehler, M. J.; Ramamurty, U.; Reddy, C. M. Remarkably Distinct Mechanical Flexibility in Three Structurally Similar Semiconducting Organic Crystals Studied by Nanoindentation and Molecular Dynamics. *Chem. Mater.* **2019**, *31* (4), 1391−1402.

(6) Hayashi, S.; Koizumi, T. Elastic Organic Crystals of a Fluorescent π-Conjugated Molecule. *Angew. Chem., Int. Ed.* **2016**, *55* (8), 2701−2704.

(7) Annadhasan, M.; Agrawal, A. R.; Bhunia, S.; Pradeep, V. V.; Zade, S. S.; Reddy, C. M.; Chandrasekar, R. Mechanophotonics: Flexible Single-Crystal Organic Waveguides and Circuits. *Angew. Chem., Int. Ed.* **2020**, *59* (33), 13852−13858.

(8) Schweicher, G.; Garbay, G.; Jouclas, R.; Vibert, F.; Devaux, F.; Geerts, Y. H. Molecular Semiconductors for Logic Operations: Dead-End or Bright Future? *Adv. Mater.* **2020**, *32* (10), 1905909.

(9) Coropceanu, V.; Cornil, J.; da Silva Filho, D. A.; Olivier, Y.; Silbey, R.; Brédas, J.-L. Charge Transport in Organic Semiconductors. *Chem. Rev.* **2007**, *107* (4), 926−952.

(10) Mas-Torrent, M.; Rovira, C. Role of Molecular Order and Solid-State Structure in Organic Field-Effect Transistors. *Chem. Rev.* **2011**, *111* (8), 4833−4856.

(11) Diao, Y.; Lenn, K. M.; Lee, W.-Y.; Blood-Forsythe, M. A.; Xu, J.; Mao, Y.; Kim, Y.; Reinspach, J. A.; Park, S.; Aspuru-Guzik, A.; Xue, G.; Clancy, P.; Bao, Z.; Mannsfeld, S. C. B. Understanding Polymorphism in Organic Semiconductor Thin Films through Nanoconfinement. *J. Am. Chem. Soc.* **2014**, *136* (49), 17046−17057.

(12) Riera-Galindo, S.; Tamayo, A.; Mas-Torrent, M. Role of Polymorphism and Thin-Film Morphology in Organic Semiconductors Processed by Solution Shearing. *ACS Omega* **2018**, *3* (2), 2329−2339.

(13) Courté, M.; Ye, J.; Jiang, H.; Ganguly, R.; Tang, S.; Kloc, C.; Fichou, D. Tuning the π-π Overlap and Charge Transport in Single Crystals of an Organic Semiconductor via Solvation and Polymorphism. *Phys. Chem. Chem. Phys.* **2020**, *22* (35), 19855−19863.

(14) Sun, Y.; Lei, Y.; Dong, H.; Zhen, Y.; Hu, W. Solvatomechanical Bending of Organic Charge Transfer Cocrystal. *J. Am. Chem. Soc.* **2018**, *140* (20), 6186−6189.

(15) Siegrist, T.; Besnard, C.; Haas, S.; Schiltz, M.; Pattison, P.; Chernyshov, D.; Batlogg, B.; Kloc, C. A Polymorph Lost and Found: The High-Temperature Crystal Structure of Pentacene. *Adv. Mater.* **2007**, *19* (16), 2079−2082.

(16) Venuti, E.; Della Valle, R. G.; Brillante, A.; Masino, M.; Girlando, A. Probing Pentacene Polymorphs by Lattice Dynamics Calculations. *J. Am. Chem. Soc.* **2002**, *124* (10), 2128−2129.

(17) Mattheus, C. C.; Dros, A. B.; Baas, J.; Oostergetel, G. T.; Meetsma, A.; de Boer, J. L.; Palstra, T. T. M. Identification of Polymorphs of Pentacene. *Synth. Met.* **2003**, *138* (3), 475−481.

(18) Giri, G.; Park, S.; Vosgueritchian, M.; Shulaker, M. M.; Bao, Z. High-Mobility, Aligned Crystalline Domains of TIPS-Pentacene with Metastable Polymorphs Through Lateral Confinement of Crystal Growth. *Adv. Mater.* **2014**, *26* (3), 487−493.

(19) Jo, P. S.; Duong, D. T.; Park, J.; Sinclair, R.; Salleo, A. Control of Rubrene Polymorphs via Polymer Binders: Applications in Organic Field-Effect Transistors. *Chem. Mater.* **2015**, *27* (11), 3979−3987.

(20) Servet, B.; Horowitz, G.; Ries, S.; Lagorsse, O.; Alnot, P.; Yassar, A.; Deloffre, F.; Srivastava, P.; Hajlaoui, R. Polymorphism and Charge Transport in Vacuum-Evaporated Sexithiophene Films. *Chem. Mater.* **1994**, *6* (10), 1809−1815.

(21) Wedl, B.; Resel, R.; Leising, G.; Kunert, B.; Salzmann, I.; Oehzelt, M.; Koch, N.; Vollmer, A.; Duhm, S.; Werzer, O.; Gbabode, G.; Sferrazza, M.; Geerts, Y. Crystallisation Kinetics in Thin Films of Dihexyl-Terthiophene: The Appearance of Polymorphic Phases. *RSC Adv.* **2012**, *2* (10), 4404−4414.

(22) Chung, H.; Chen, S.; Patel, B.; Garbay, G.; Geerts, Y. H.; Diao, Y. Understanding the Role of Bulky Side Chains on Polymorphism of BTBT-Based Organic Semiconductors. *Cryst. Growth Des.* **2020**, *20* (3), 1646−1654.

(23) Chung, H.; Chen, S.; Sengar, N.; Davies, D. W.; Garbay, G.; Geerts, Y. H.; Clancy, P.; Diao, Y. Single Atom Substitution Alters the Polymorphic Transition Mechanism in Organic Electronic Crystals. *Chem. Mater.* **2019**, *31* (21), 9115–9126.

(24) Hiszpanski, A. M.; Baur, R. M.; Kim, B.; Tremblay, N. J.; Nuckolls, C.; Woll, A. R.; Loo, Y.-L. Tuning Polymorphism and Orientation in Organic Semiconductor Thin Films via Post-Deposition Processing. *J. Am. Chem. Soc.* **2014**, *136* (44), 15749–15756.

(25) Schweicher, G.; Lemaur, V.; Niebel, C.; Ruzié, C.; Diao, Y.; Goto, O.; Lee, W.; Kim, Y.; Arlin, J.; Karpinska, J.; Kennedy, A. R.; Parkin, S. R.; Olivier, Y.; Mannsfeld, S. C. B.; Cornil, J.; Geerts, Y. H.; Bao, Z. Bulky End-Capped [1]Benzothieno[3,2- *b*]Benzothiophenes: Reaching High-Mobility Organic Semiconductors by Fine Tuning of the Crystalline Solid-State Order. *Adv. Mater.* **2015**, *27* (19), 3066–3072.

(26) Bernstein, J. *Polymorphism in Molecular Crystals 2e; International Union of Crystal*; Oxford University Press, 2020.

(27) Schweicher, G.; Olivier, Y.; Lemaur, V.; Geerts, Y. H. What Currently Limits Charge Carrier Mobility in Crystals of Molecular Semiconductors? *Isr. J. Chem.* **2014**, *54* (5–6), 595–620.

(28) Cruz-Cabeza, A. J.; Bernstein, J. Conformational Polymorphism. *Chem. Rev.* **2014**, *114* (4), 2170–2191.

(29) Schmidt, M. U.; Brüning, J.; Glinnemann, J.; Hützler, M. W.; Mörschel, P.; Ivashevskaya, S. N.; van de Streek, J.; Braga, D.; Maini, L.; Chierotti, M. R.; Gobetto, R. The Thermodynamically Stable Form of Solid Barbituric Acid: The Enol Tautomer. *Angew. Chem., Int. Ed.* **2011**, *50* (34), 7924–7926.

(30) Mortazavi, M.; Hoja, J.; Aerts, L.; Quéré, L.; van de Streek, J.; Neumann, M. A.; Tkatchenko, A. Computational Polymorph Screening Reveals Late-Appearing and Poorly-Soluble Form of Rotigotine. *Communications Chemistry* **2019**, *2* (1), 70.

(31) Bofill, L.; de Sande, D.; Barbas, R.; Frontera, A.; Prohens, R. A Late Appearing Polymorph of Nutraceutical Pterostilbene. *CrystEngComm* **2020**, *22* (28), 4680–4684.

(32) Fernández, A. B.; Garcez da Veiga, A.; Aliev, A.; Ruzié, C.; Garbay, G.; Chattopadhyay, B.; Kennedy, A. R.; Geerts, Y. H.; Rocco, M. L. M. [1]Benzothieno[3,2-b]Benzothiophene (BTBT) Derivatives: Influence in the Molecular Orientation and Charge Delocalization Dynamics. *Mater. Chem. Phys.* **2019**, *221*, 295–300.

(33) Inoue, S.; Minemawari, H.; Tsutsumi, J.; Chikamatsu, M.; Yamada, T.; Horiuchi, S.; Tanaka, M.; Kumai, R.; Yoneya, M.; Hasegawa, T. Effects of Substituted Alkyl Chain Length on Solution-Processable Layered Organic Semiconductor Crystals. *Chem. Mater.* **2015**, *27* (11), 3809–3812.

(34) Jones, A. O. F.; Geerts, Y. H.; Karpinska, J.; Kennedy, A. R.; Resel, R.; Röthel, C.; Ruzié, C.; Werzer, O.; Sferrazza, M. Substrate-Induced Phase of a [1]Benzothieno[3,2- *b*]Benzothiophene Derivative and Phase Evolution by Aging and Solvent Vapor Annealing. *ACS Appl. Mater. Interfaces* **2015**, *7* (3), 1868–1873.

(35) Gbabode, G.; Dohr, M.; Niebel, C.; Balandier, J.-Y.; Ruzié, C.; Négrier, P.; Mondieig, D.; Geerts, Y. H.; Resel, R.; Sferrazza, M. X-Ray Structural Investigation of Nonsymmetrically and Symmetrically Alkylated [1]Benzothieno[3,2-b]Benzothiophene Derivatives in Bulk and Thin Films. *ACS Appl. Mater. Interfaces* **2014**, *6* (16), 13413–13421.

(36) Minemawari, H.; Tanaka, M.; Tsuzuki, S.; Inoue, S.; Yamada, T.; Kumai, R.; Shimoi, Y.; Hasegawa, T. Enhanced Layered-Herringbone Packing Due to Long Alkyl Chain Substitution in Solution-Processable Organic Semiconductors. *Chem. Mater.* **2017**, *29* (3), 1245–1254.

(37) Pérez-Rodríguez, A.; Temiño, I.; Ocal, C.; Mas-Torrent, M.; Barrena, E. Decoding the Vertical Phase Separation and Its Impact on C8-BTBT/PS Transistor Properties. *ACS Appl. Mater. Interfaces* **2018**, *10* (8), 7296–7303.

(38) Haase, K.; Teixeira da Rocha, C.; Hauenstein, C.; Zheng, Y.; Hambsch, M.; Mannsfeld, S. High-Mobility, Solution-Processed Organic Field-Effect Transistors from C8-BTBT:Polystyrene Blends. *Advanced Electronic Materials* **2018**, *4*, 1800076.

(39) Cappuccino, C.; Mazzeo, P. P.; Salzillo, T.; Venuti, E.; Giunchi, A.; Della Valle, R. G.; Brillante, A.; Bettini, C.; Melucci, M.; Maini, L. A Synergic Approach of X-Ray Powder Diffraction and Raman Spectros-

(40) Cappuccino, C.; Catalano, L.; Marin, F.; Dushaq, G.; Raj, G.; Rasras, M.; Rezgui, R.; Zambianchi, M.; Melucci, M.; Naumov, P.; Maini, L. Structure-Mechanical Relationships in Polymorphs of an Organic Semiconductor (C4-NT3N). *Cryst. Growth Des.* **2020**, *20* (2), 884–891.

(41) Das, S.; Mondal, A.; Reddy, C. M. Harnessing Molecular Rotations in Plastic Crystals: A Holistic View for Crystal Engineering of Adaptive Soft Materials. *Chem. Soc. Rev.* **2020**, *49* (24), 8878–8896.

(42) Chattoraj, S.; Shi, L.; Sun, C. C. Understanding the Relationship between Crystal Structure, Plasticity and Compaction Behaviour of Theophylline, Methyl Gallate, and Their 1:1 Co-Crystal. *CrystEngComm* **2010**, *12* (8), 2466–2472.

(43) Sun, C. C.; Hou, H. Improving Mechanical Properties of Caffeine and Methyl Gallate Crystals by Cocrystallization. *Cryst. Growth Des.* **2008**, *8* (5), 1575–1579.

(44) Griesser, U. J. The Importance of Solvates. In *Polymorphism*; John Wiley & Sons, Ltd, 2006; pp 211–233. DOI: 10.1002/3527607889.ch8.

(45) Lausi, A.; Polentarutti, M.; Onesti, S.; Plaisier, J. R.; Busetto, E.; Bais, G.; Barba, L.; Cassetta, A.; Campi, G.; Lamba, D.; Pifferi, A.; Mande, S. C.; Sarma, D. D.; Sharma, S. M.; Paolucci, G. Status of the Crystallography Beamlines at Elettra. *European Physical Journal Plus* **2015**, *130* (3), 43.

(46) Mueller, U.; Thunnissen, M.; Nan, J.; Eguiraun, M.; Bolmsten, F.; Milàn-Otero, A.; Guijarro, M.; Oscarsson, M.; de Sanctis, D.; Leonard, G. MXCuBE3: A New Era of MX-Beamline Control Begins. *null* **2017**, *30* (1), 22–27.

(47) Macrae, C. F.; Bruno, I. J.; Chisholm, J. A.; Edgington, P. R.; McCabe, P.; Pidcock, E.; Rodriguez-Monge, L.; Taylor, R.; van de Streek, J.; Wood, P. A. It Mercury CSD 2.0 - New Features for the Visualization and Investigation of Crystal Structures. *J. Appl. Crystallogr.* **2008**, *41* (2), 466–470.

(48) Macrae, C. F.; Sovago, I.; Cottrell, S. J.; Galek, P. T. A.; McCabe, P.; Pidcock, E.; Platings, M.; Shields, G. P.; Stevens, J. S.; Towler, M.; Wood, P. A. It Mercury 4.0: From Visualization to Analysis, Design and Prediction. *J. Appl. Crystallogr.* **2020**, *53* (1), 226–235.

(49) Willmott, P. R.; Meister, D.; Leake, S. J.; Lange, M.; Bergamaschi, A.; Boge, M.; Calvi, M.; Cancellieri, C.; Casati, N.; Cervellino, A.; Chen, Q.; David, C.; Flechsig, U.; Gozzo, F.; Henrich, B.; Jaggi-Spielmann, S.; Jakob, B.; Kalichava, I.; Karvinen, P.; Krempasky, J.; Ludeke, A.; Luscher, R.; Maag, S.; Quitmann, C.; Reinle-Schmitt, M. L.; Schmidt, T.; Schmitt, B.; Streun, A.; Vartiainen, I.; Vitins, M.; Wang, X.; Wullschleger, R. The Materials Science Beamline Upgrade at the Swiss Light Source. *J. Synchrotron Radiation* **2013**, 667–682, DOI: 10.1107/S0909049513018475.

(50) Bruno, I. J.; Cole, J. C.; Kessler, M.; Luo, J.; Motherwell, W. D. S.; Purkis, L. H.; Smith, B. R.; Taylor, R.; Cooper, R. I.; Harris, S. E.; Orpen, A. G. Retrieval of Crystallographically-Derived Molecular Geometry Information. *J. Chem. Inf. Comput. Sci.* **2004**, *44* (6), 2133–2144.

(51) Macrae, C. F.; Edgington, P. R.; McCabe, P.; Pidcock, E.; Shields, G. P.; Taylor, R.; Towler, M.; van de Streek, J. It Mercury: Visualization and Analysis of Crystal Structures. *J. Appl. Crystallogr.* **2006**, *39* (3), 453–457.

(52) Spackman, M. A.; Jayatilaka, D. Hirshfeld Surface Analysis. *CrystEngComm* **2009**, *11* (1), 19–32.

(53) Scarlett, N. V. Y.; Madsen, I. C. Quantification of Phases with Partial or No Known Crystal Structures. *Powder Diffraction* **2006**, *21* (4), 278–284.

(54) Hill, R. J.; Howard, C. J. Quantitative Phase Analysis from Neutron Powder Diffraction Data Using the Rietveld Method. *J. Appl. Crystallogr.* **1987**, *20* (6), 467–474.

(55) Avrami, M. Kinetics of Phase Change. I General Theory. *J. Chem. Phys.* **1939**, *7* (12), 1103–1112.

(56) Avrami, M. Granulation, Phase Change, and Microstructure Kinetics of Phase Change. III. *J. Chem. Phys.* **1941**, *9* (2), 177–184.

copy for Crystal Structure Determination of 2,3-Thienoimide Capped Oligothiophenes. *Phys. Chem. Chem. Phys.* **2018**, *20* (5), 3630–3636.

(57) Müller, M.; Dinnebier, R. E.; Jansen, M.; Wiedemann, S.; Plüg, C. Kinetic Analysis of the Phase Transformation from α- to β-Copper Phthalocyanine: A Case Study for Sequential and Parametric Rietveld Refinements. *Powder Diffraction* **2009**, *24* (3), 191−199.

(58) Das, S. Harnessing Molecular Rotations in Plastic Crystals: A Holistic View for Crystal Engineering of Adaptive Soft Materials. *Chem. Soc. Rev.* **2020**, 19.

(59) Mackenzie, C. F.; Spackman, P. R.; Jayatilaka, D.; Spackman, M. A. *CrystalExplorer* Model Energies and Energy Frameworks: Extension to Metal Coordination Compounds, Organic Salts, Solvates and Open-Shell Systems. *IUCrJ.* **2017**, *4* (5), 575−587.

(60) Turner, M. J.; Thomas, S. P.; Shi, M. W.; Jayatilaka, D.; Spackman, M. A. Energy Frameworks: Insights into Interaction Anisotropy and the Mechanical Properties of Molecular Crystals. *Chem. Commun.* **2015**, *51* (18), 3735−3738.

(61) Thomas, S. P.; Shi, M. W.; Koutsantonis, G. A.; Jayatilaka, D.; Edwards, A. J.; Spackman, M. A. The Elusive Structural Origin of Plastic Bending in Dimethyl Sulfone Crystals with Quasi-Isotropic Crystal Packing. *Angew. Chem., Int. Ed.* **2017**, *56* (29), 8468−8472.

(62) Wang, C.; Paul, S.; Sun, D. J.; Nilsson Lill, S. O.; Sun, C. C. Mitigating Punch Sticking Propensity of Celecoxib by Cocrystallization: An Integrated Computational and Experimental Approach. *Cryst. Growth Des.* **2020**, *20* (7), 4217−4223.

(63) Halme, A.; Quayle, M. J.; Nilsson Lill, S. O.; Pettersen, A.; Fransson, M.; Boissier, C. Utilizing Crystal Structures for Predicting Impact of Mechanical and Surface Properties on Particle Fracture. *Cryst. Growth Des.* **2019**, *19* (7), 3670−3680.

(64) Reddy, C. M.; Padmanabhan, K. A.; Desiraju, G. R. Structure-Property Correlations in Bending and Brittle Organic Crystals. *Cryst. Growth Des.* **2006**, *6* (12), 2720−2731.

(65) Tsutsui, Y.; Schweicher, G.; Chattopadhyay, B.; Sakurai, T.; Arlin, J.-B.; Ruzié, C.; Aliev, A.; Ciesielski, A.; Colella, S.; Kennedy, A. R.; Lemaur, V.; Olivier, Y.; Hadji, R.; Sanguinet, L.; Castet, F.; Osella, S.; Dudenko, D.; Beljonne, D.; Cornil, J.; Samorì, P.; Seki, S.; Geerts, Y. H. Unraveling Unprecedented Charge Carrier Mobility through Structure Property Relationship of Four Isomers of Didodecyl[1]-Benzothieno[3,2-b][1]Benzothiophene. *Adv. Mater.* **2016**, *28* (33), 7106−7114.